Supplement

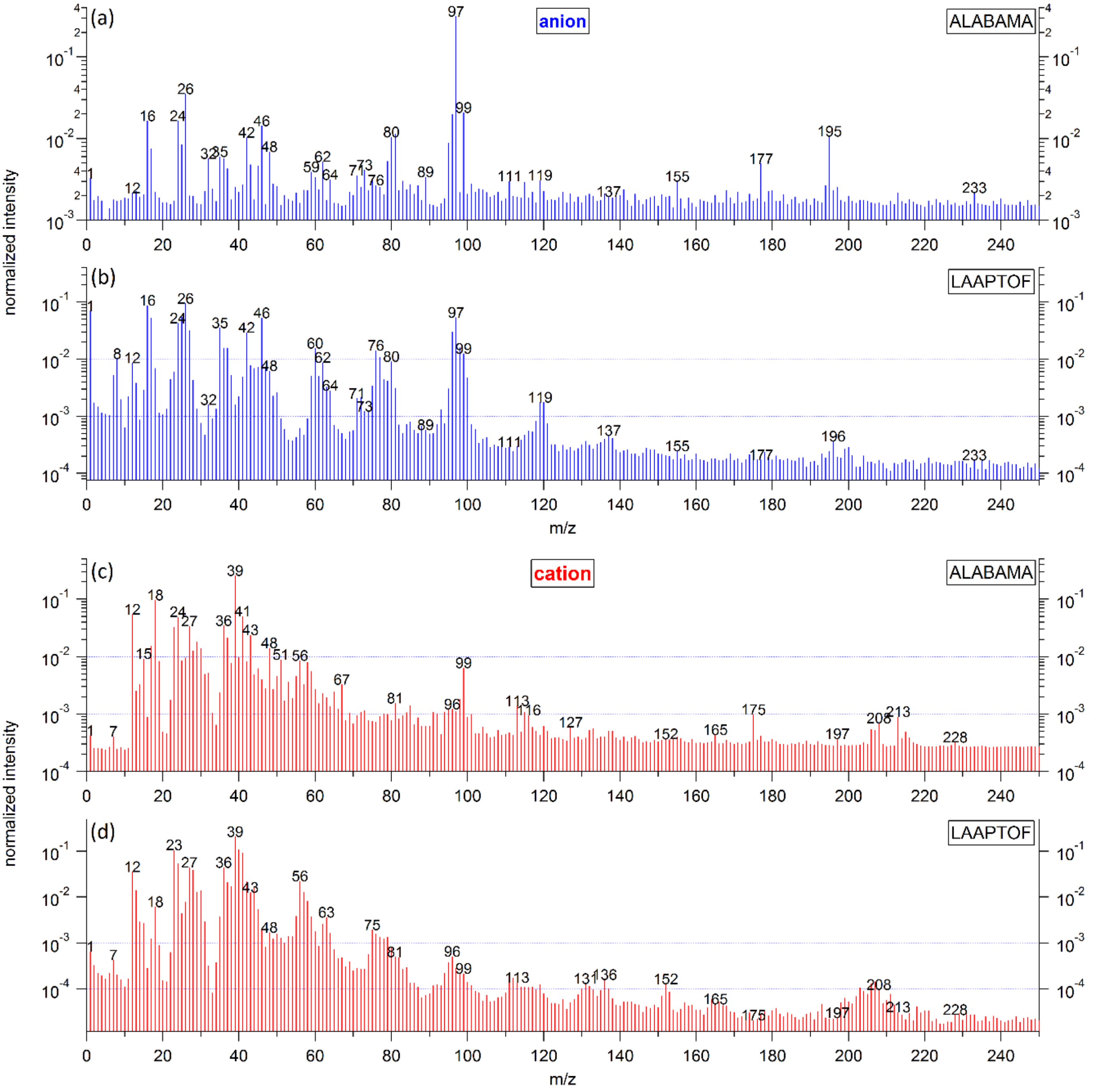

Figure S1: Comparison of the averaged anion and cation mass spectra detected by ALABAMA (panel a, c) and LAAPTOF (panel b, d) over a period of 24 hours with parallel sampling (12:00 14.02.2017 - 12:00 15.02.2017). The number of averaged mass spectra is 146498 for the ALABAMA and 4709 for the LAAPTOF. A correlation of the two averaged mass spectra results in a spearman´s rank correlation coefficient of 0.81 for the anion mass spectra, and of 0.59 for the cation mass spectra.

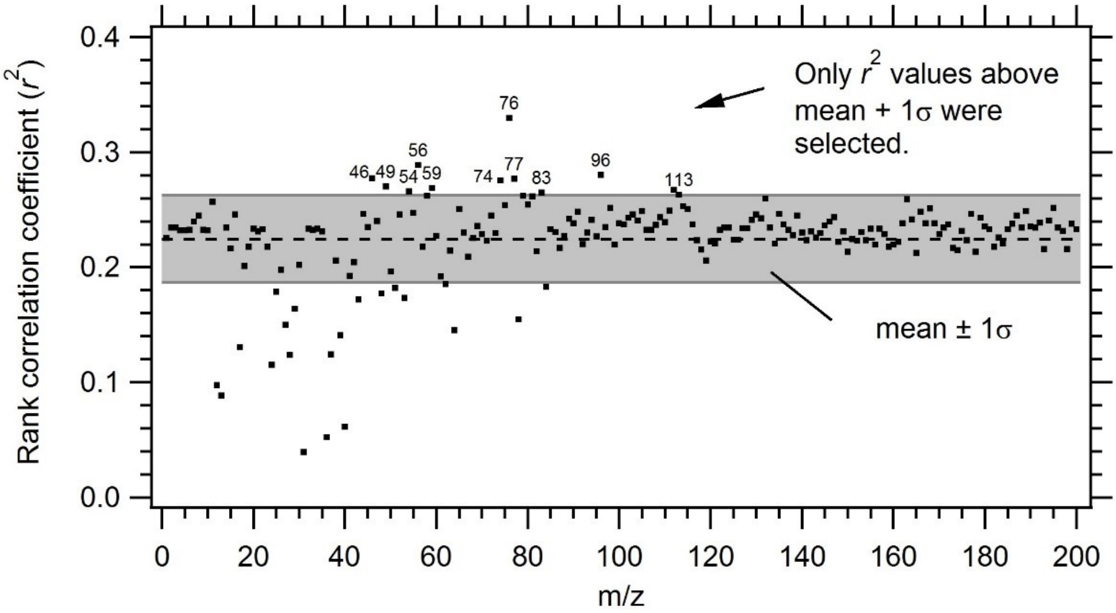

Figure S2: Squared ranked correlation coefficients (r^2) for INP concentrations with the m/z ratios from ALABAMA; we consider a coefficient (r) to be meaningful only when the r^2 is above the mean ± 1 standard deviation (1σ) outside the grey shaded region).

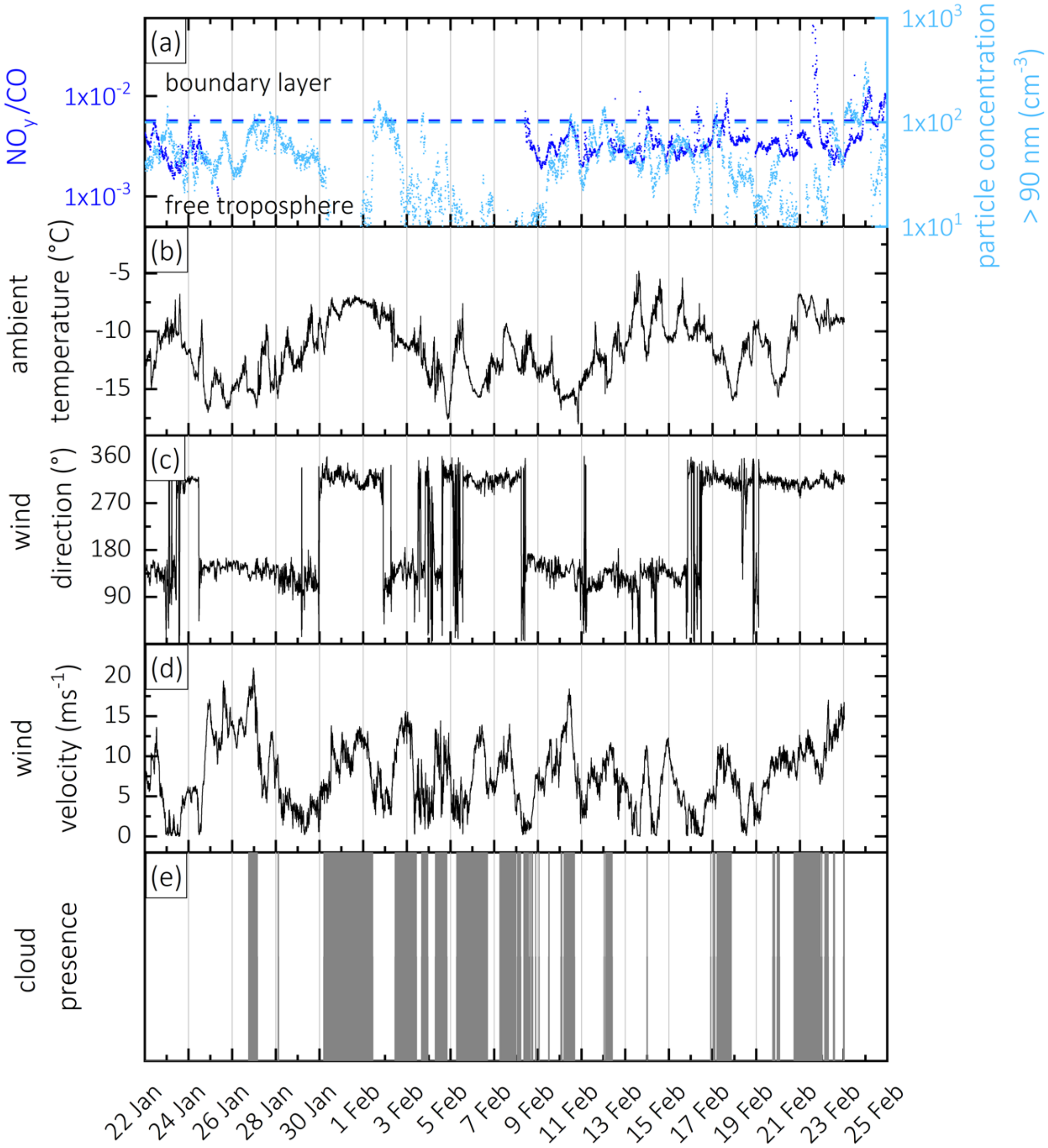

Figure S3: Timeseries of (panel a) reactive nitrogen to carbon monoxide ratio (NO_y/CO) and particle concentration > 90 nm to distinguish free tropospheric sampling conditions at JFJ, dashed line represents threshold values 0.0057 (NO_y/CO; Zellweger et al., 2003) and 100 cm^{-3} (particle concentration >90 nm, Herrmann et al., 2015), below which the station is in the free troposphere; (panel b) ambient temperature; (panel c) wind direction; (panel d) wind velocity; (panel e) cloud presence.

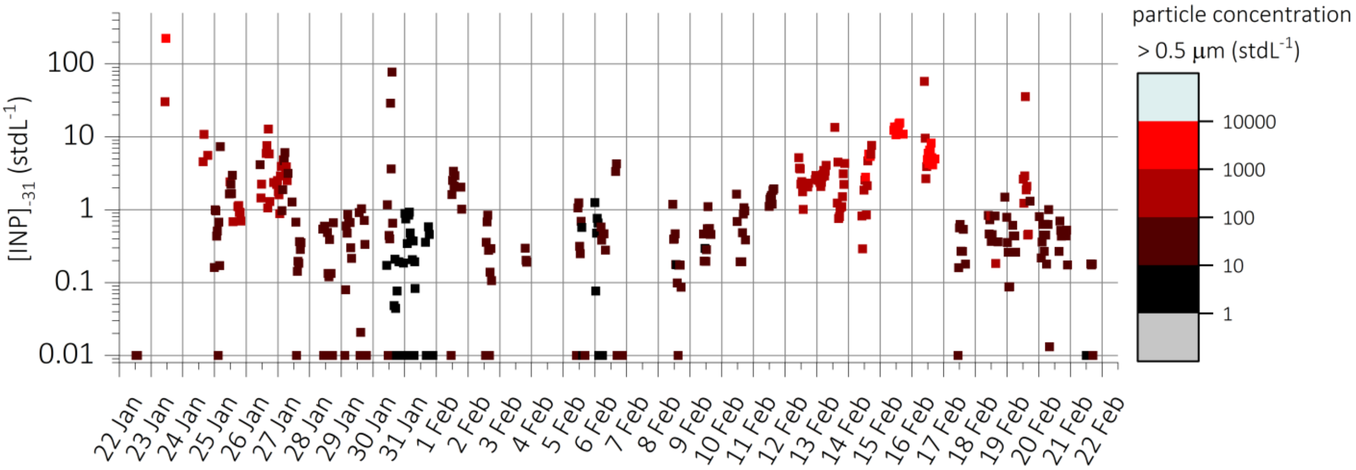

Figure S4: Timeseries of $[\mathrm{INP}]_{-31}$ color coded according to particle concentration > 0.5 µm (stdL^{-1}) showing elevated INP concentrations between January 22 – 27 and February 11 – 17 occur simultaneously with a higher fraction of larger particles.

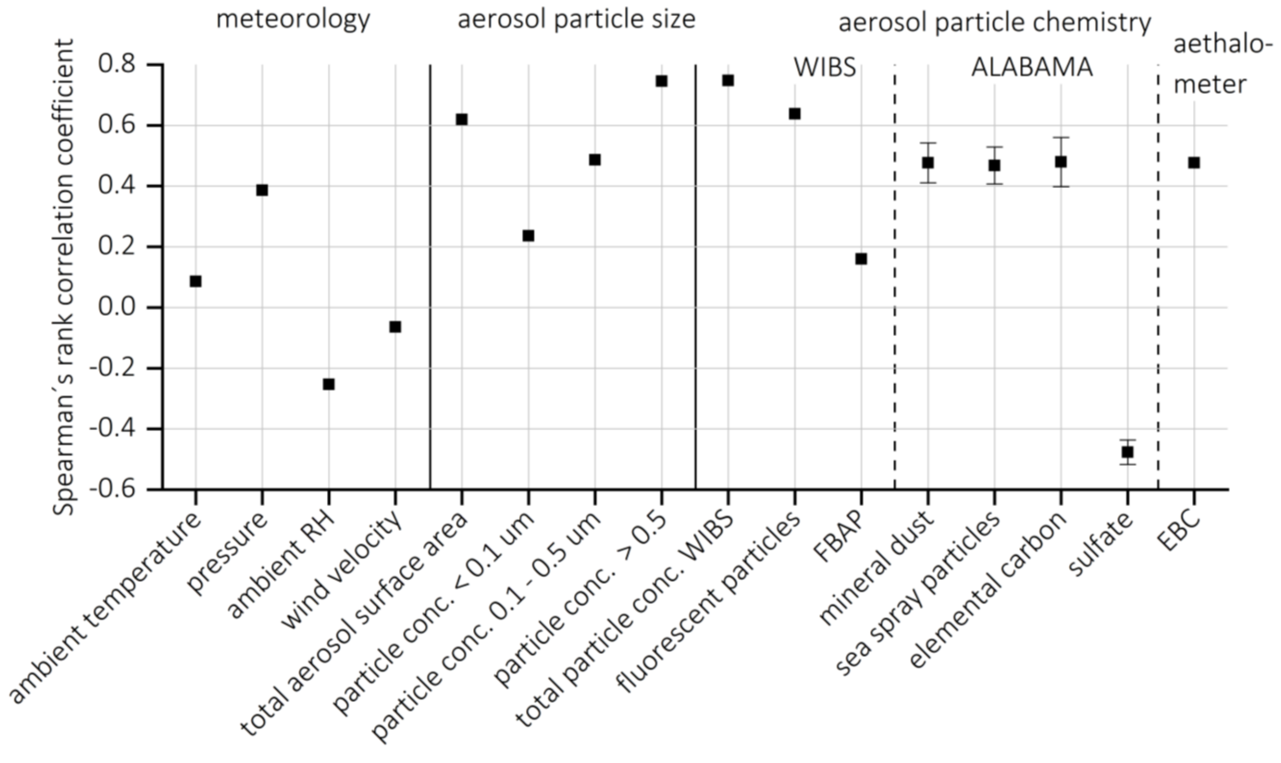

Figure S5: Spearman´s rank correlation coefficients for $[\mathrm{INP}]_{-31}$ (>LOD) with meteorological parameters, aerosol size distribution measurements, and aerosol particle chemistry determined with the WIBS (concentration all particles, fluorescent aerosol particles (FAP) and fluorescent biological aerosol particles (FBAP) within the size range of the instrument (> 0.5 µm)), the ALABAMA (mineral dust, sea spray particles, elemental carbon, sulfate, see section 3.3, error bar represents the standard deviation) and with the aethalometer (elemental black carbon, eBC).

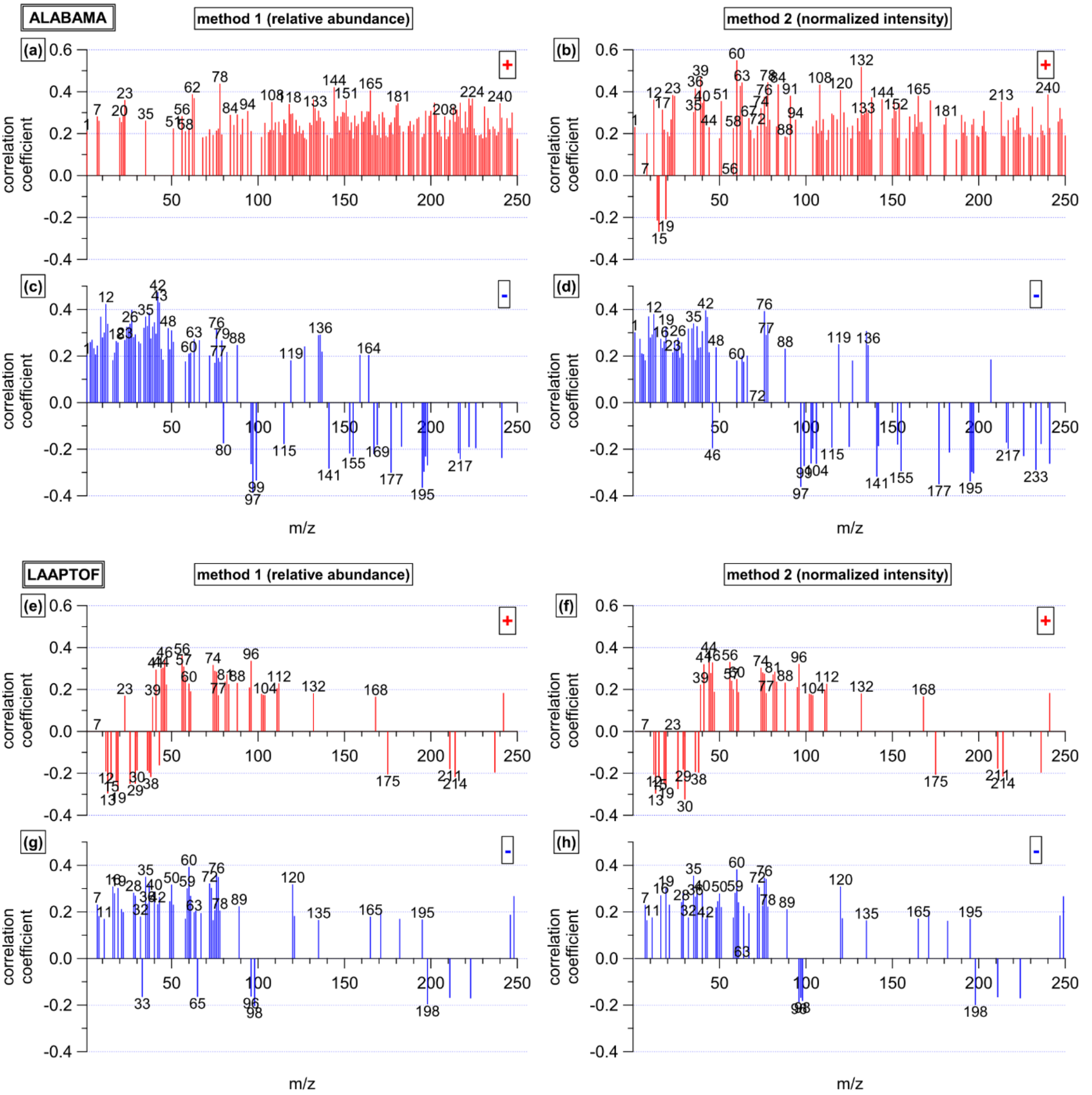

Figure S6: ALABAMA (panels a - d) and LAAPTOF (panels e - h) correlation coefficients of ions with n_s for method 1 (fraction of mass spectra containing a given ion) and 2 (relative ion signal).

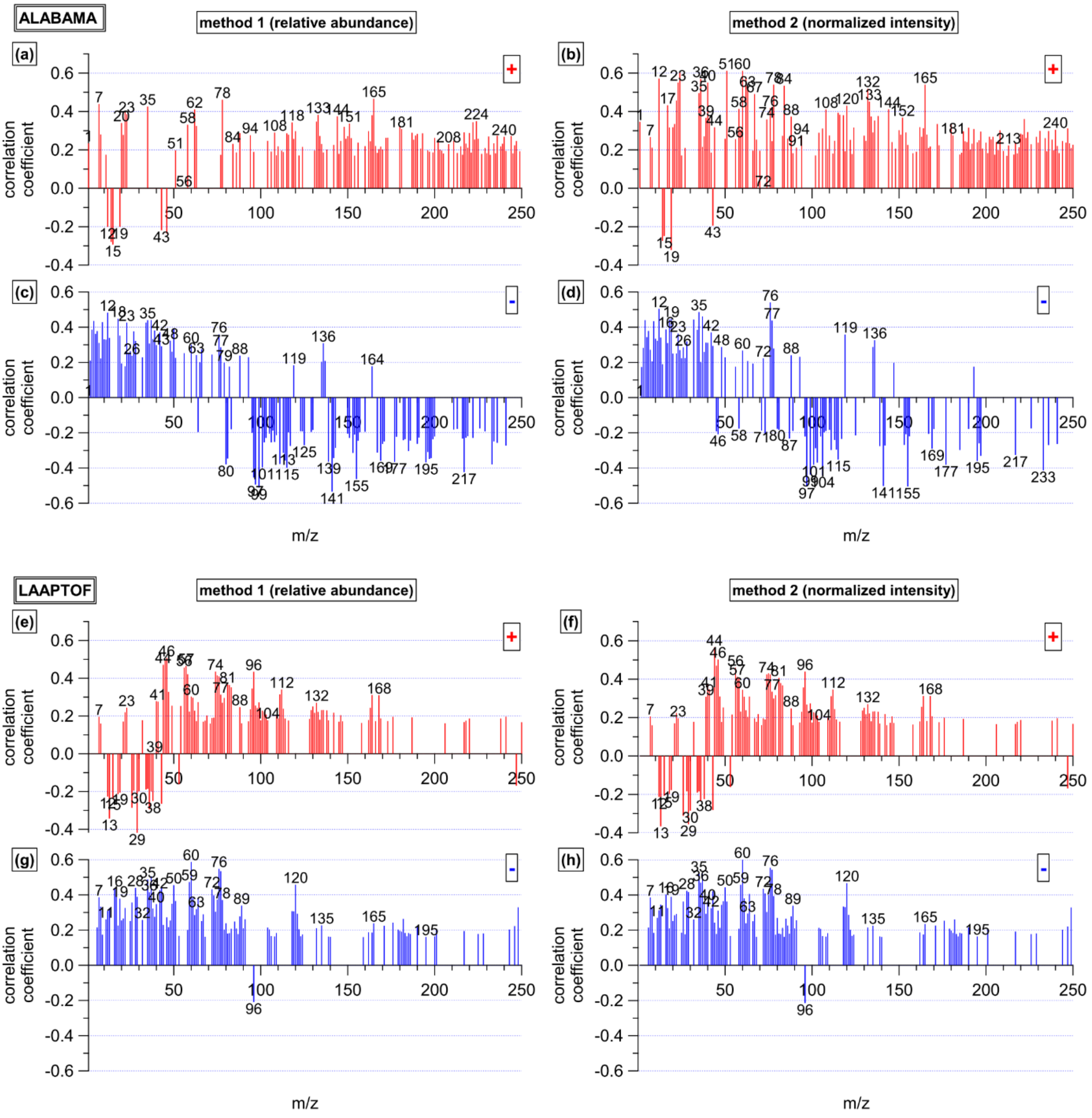

Figure S7: ALABAMA (panels a-d) and LAAPTOF (panels e - h) correlation coefficients of ions with $[INP]_{-31}$ for method 1 (fraction of mass spectra containing a given ion) and 2 (relative ion signal).

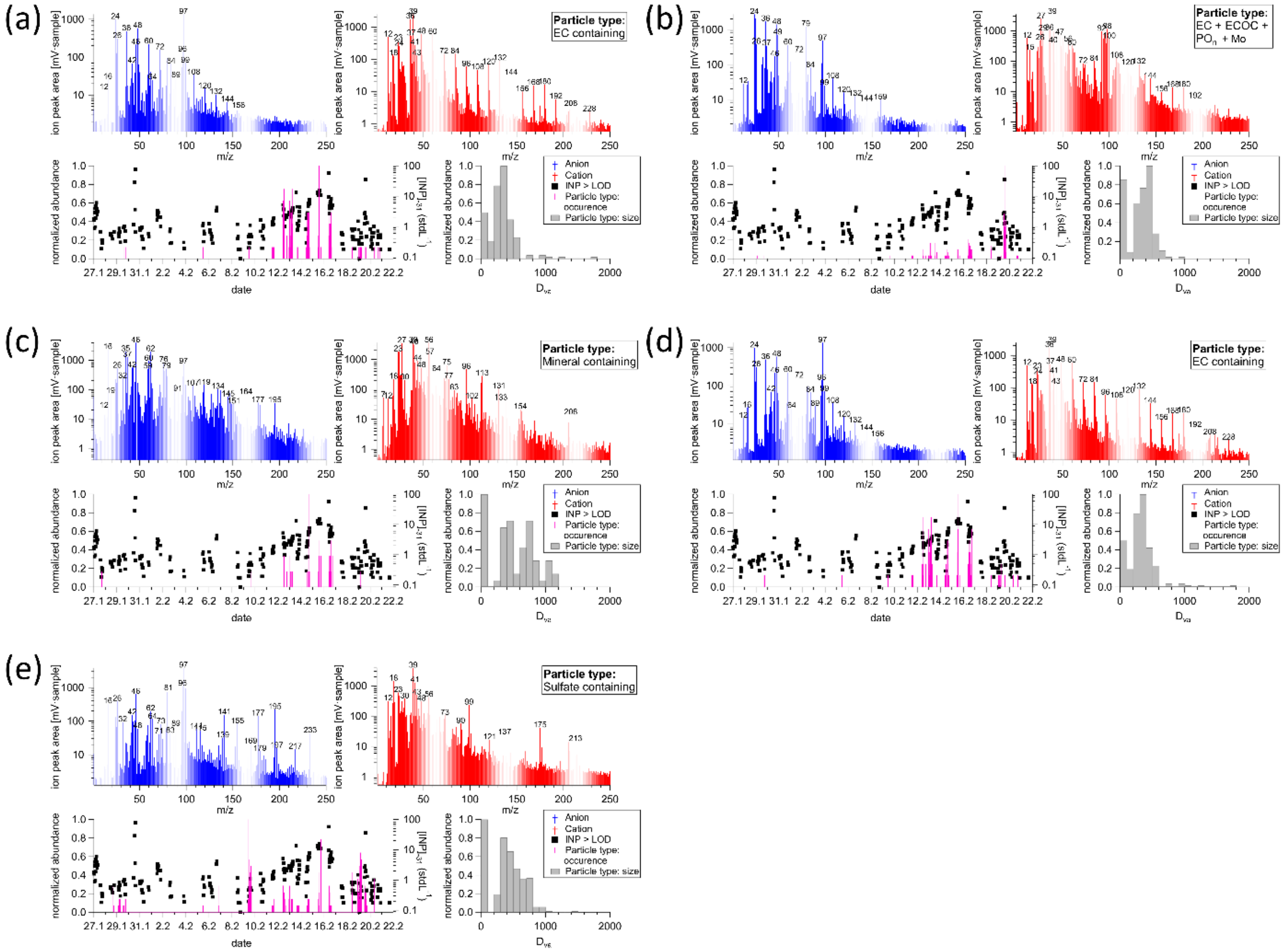

Figure S8: ALABAMA reference spectra for the identified EC-containing particle type (panel a), EC-containing particle type internally mixed with ECOC, phosphate and molybdenum (panel b), mineral dust (panel c), the identified aged sea spray containing particle type (panel d), and sulfate containing particles (panel e). Presented are the anion (blue) and the cation (red) mass spectra, as well as the normalized time series and the size distribution of this particle type.

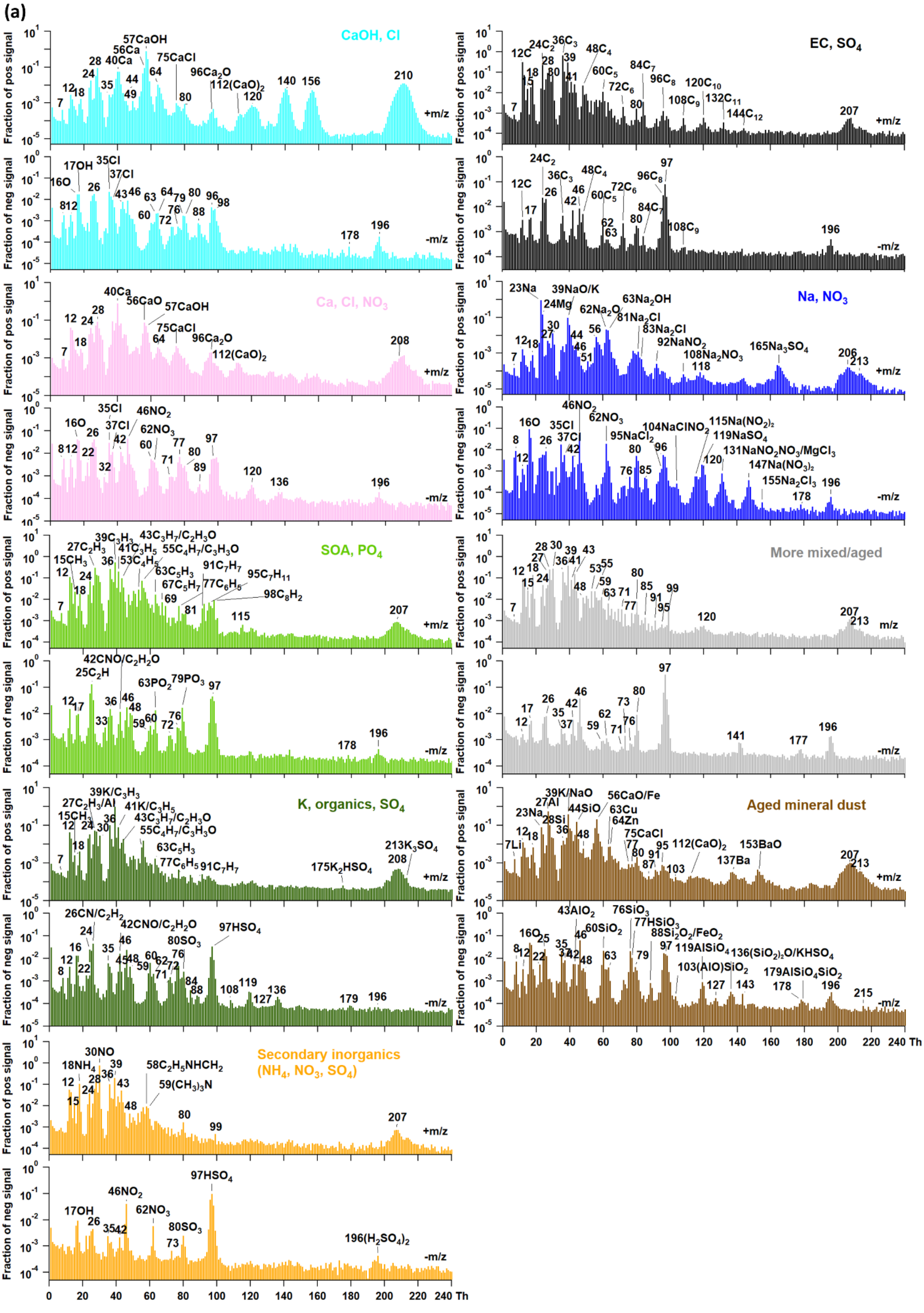
(a)
CaOH, Cl
7
12
18
24
28
35
40Ca
44
49
56Ca
57CaOH
64
75CaCl
80
96Ca2O
112(CaO)2
120
140
156
210
+m/z
8
12
16O
17OH
26
35Cl
37Cl
43
46
60
63
64
72
76
79
80
88
96
98
178
196
-m/z
EC, SO4
7
12C
15
18
24C2
28
30
36C3
39
41
48C4
60C5
72C6
80
84C7
96C8
108C9
120C10
132C11
144C12
207
+m/z
12C
17
24C2
26
36C3
42
46
48C4
60C5
62
63
72C6
80
84C7
96C8
97
108C9
196
-m/z
Ca, Cl, NO3
7
12
18
24
28
40Ca
56CaO
57CaOH
64
75CaCl
96Ca2O
112(CaO)2
208
+m/z
8
12
16O
22
26
32
35Cl
37Cl
42
46NO2
60
62NO3
71
77
80
89
97
120
136
196
-m/z
Na, NO3
7
12
18
23Na
24Mg
27
30
39NaO/K
44
46
51
56
62Na2O
63Na2OH
81Na2Cl
83Na2Cl
92NaNO2
108Na2NO3
118
165Na3SO4
206
213
+m/z
8
12
16O
26
35Cl
37Cl
42
46NO2
62NO3
76
80
85
95NaCl2
96
104NaClNO2
115Na(NO2)2
119NaSO4
120
131NaNO2NO3/MgCl3
147Na(NO3)2
155Na2Cl3
178
196
-m/z
SOA, PO4
7
12
15CH3
18
24
27C2H3
36
39C3H3
41C3H5
43C3H7/C2H3O
53C4H5
55C4H7/C3H3O
63C5H3
67C5H7
69
77C6H5
81
91C7H7
95C7H11
98C8H2
115
207
+m/z
12
17
25C2H
33
36
42CNO/C2H2O
46
48
59
60
63PO2
72
76
79PO3
97
178
196
-m/z
More mixed/aged
7
12
15
18
24
27
28
30
36
39
41
43
48
53
55
59
63
71
77
80
85
91
95
99
120
207
213
m/z
12
17
26
35
37
42
46
59
62
71
73
76
80
97
141
177
196
-m/z
K, organics, SO4
7
12
15CH3
18
24
27C2H3/Al
30
36
39K/C3H3
41K/C3H5
43C3H7/C2H3O
55C4H7/C3H3O
63C5H3
77C6H5
91C7H7
175K2HSO4
208
213K3SO4
+m/z
8
12
16
22
24
26CN/C2H2
35
42CNO/C2H2O
45
46
48
59
60
62
71
72
76
80SO3
84
88
97HSO4
108
119
127
136
179
196
-m/z
Aged mineral dust
7Li
12
18
23Na
27Al
28Si
36
39K/NaO
44SiO
48
56CaO/Fe
63Cu
64Zn
75CaCl
77
80
87
91
95
103
112(CaO)2
137Ba
153BaO
207
213
+m/z
8
12
16O
22
25
35
37
42
43AlO2
46
48
60SiO2
63
76SiO3
77HSiO3
79
88Si2O2/FeO2
97
103(AlO)SiO2
119AlSiO4
127
136(SiO2)2O/KHSO4
143
178
179AlSiO4SiO2
196
215
-m/z
Secondary inorganics (NH4, NO3, SO4)
12
15
18NH4
24
28
30NO
36
39
43
48
58C2H5NHCH2
59(CH3)3N
80
99
207
+m/z
17OH
26
35
42
46NO2
62NO3
73
80SO3
97HSO4
196(H2SO4)2
-m/z
Fraction of pos signal
Fraction of neg signal
10^1
10^0
10^-1
10^-2
10^-3
10^-4
10^-5
0
20
40
60
80
100
120
140
160
180
200
220
240 Th

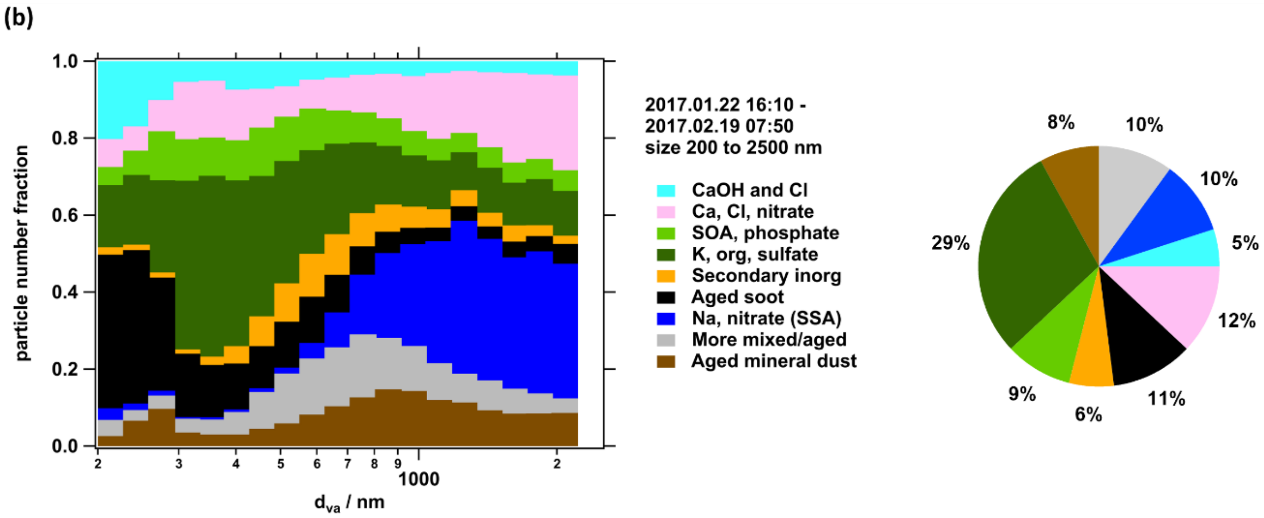

Figure S9: Representative mass spectra (panel a) of nine ambient particle classes measured during the field campaign INUIT-CLACE-2017 from January 22 to February 22, 2017. 26360 particles were detected and successfully ablated by LAAPTOF, resulting in corresponding mass spectra and size. The size resolved number fraction for nine particle classes is shown in panel (b). The percentage in the pie chart gives us information about the similarity of the total aerosols to different classes.

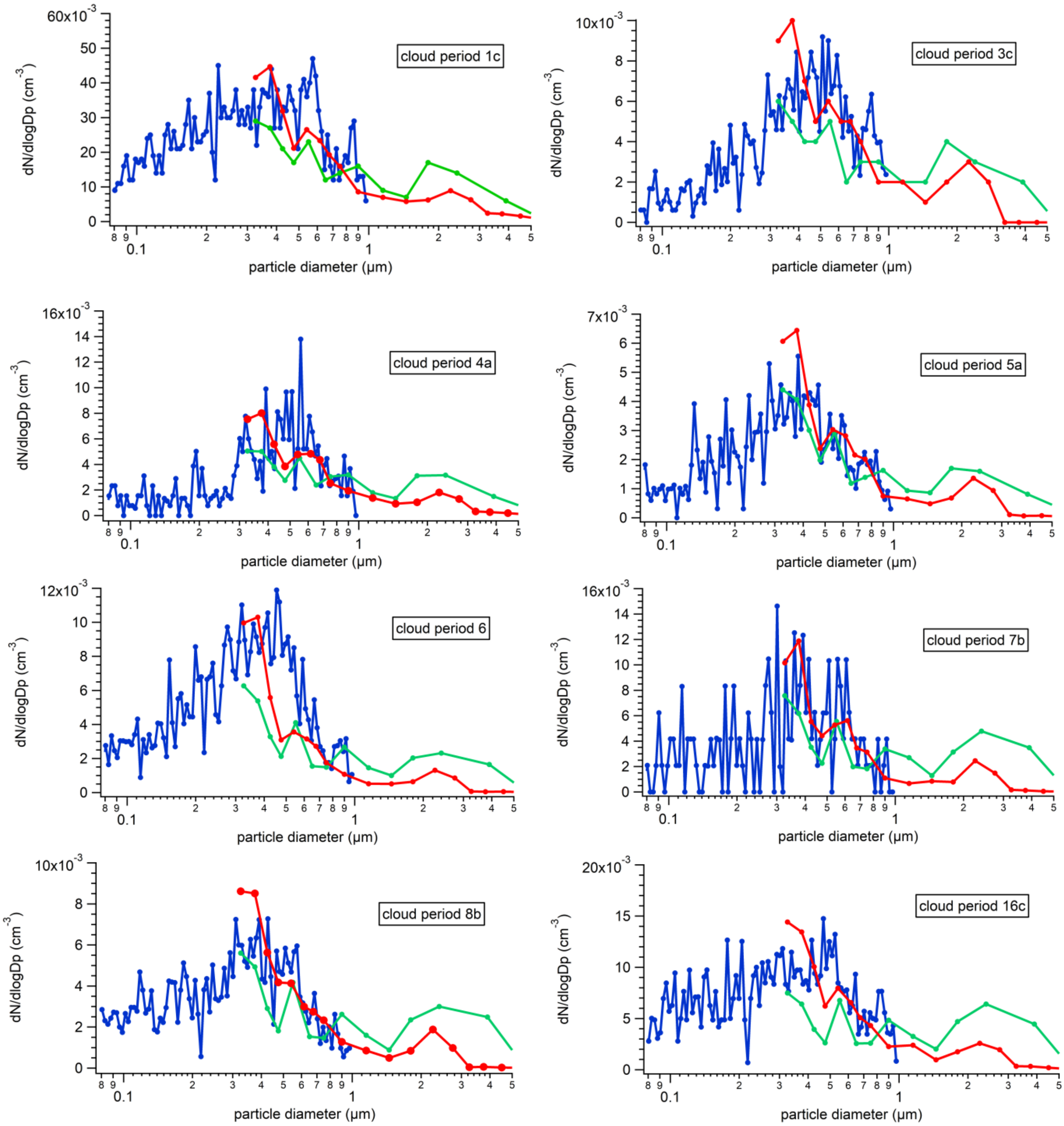

Figure S10: IPR number size distributions measured by UHSAS (blue), OPS (green) and Sky-OPC (red) during the indicated cloud periods (cf. Tab. A2). Due to the shape of the UHSAS number size distribution (*R* > 3, low fraction of small IPR) it is concluded that the relative contribution of secondary ice is reduced.

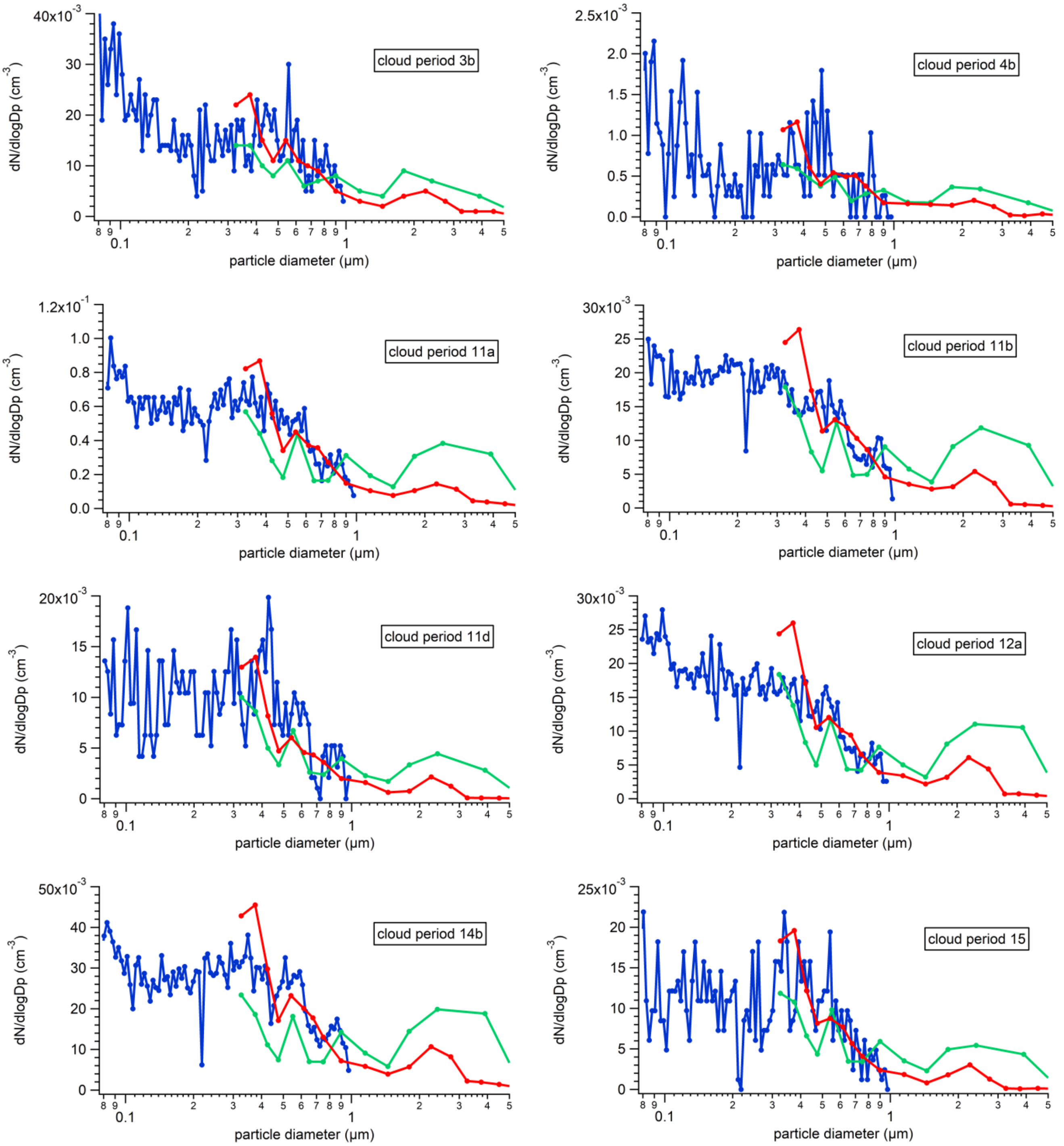

Figure S11: IPR number size distributions measured by UHSAS (blue), OPS (green) and Sky-OPC (red) during the indicated cloud periods (cf. Tab. A3). Due to the shape of the UHSAS number size distribution (*R* < 1, high fraction of small IPR) it is concluded that the relative contribution of secondary ice is enhanced.

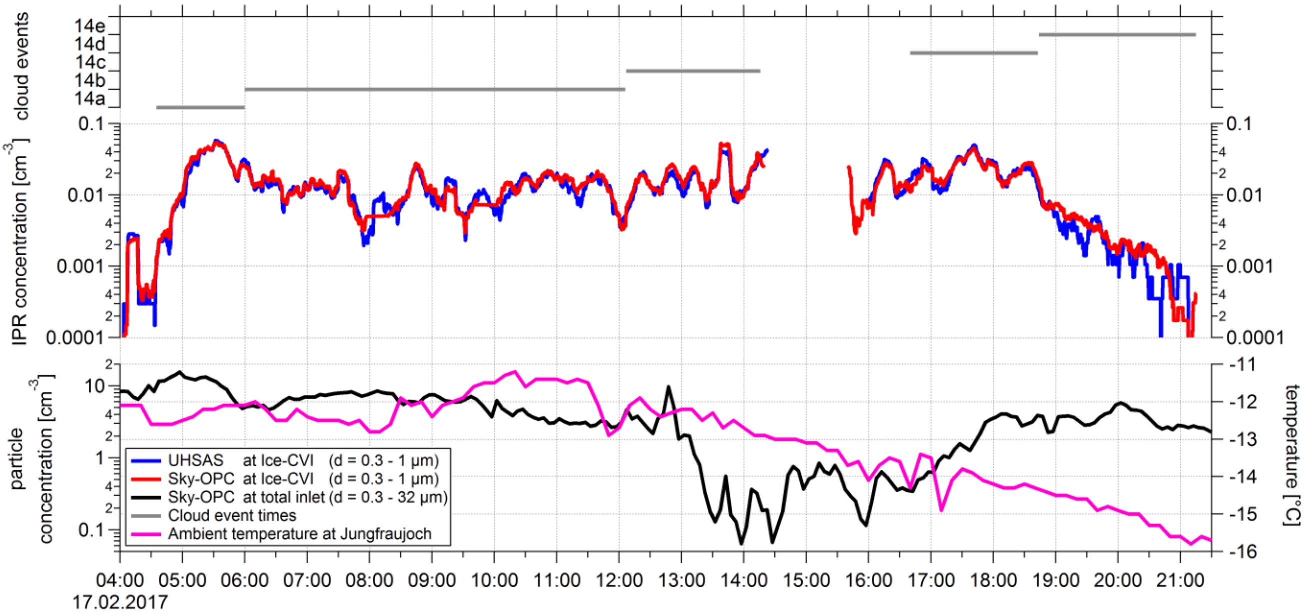

Figure S12: Time series of the IPR concentration in the size range 0.3 – 1.0 µm during cloud event 14. The IPR concentration is calculated from the UHSAS and Sky-OPC measurements downstream of the Ice-CVI (blue and red lines, respectively). The total ambient particle concentration in the size range 0.3 – 1.0 µm is calculated from the Sky-OPC measurements downstream of the total inlet (black line). The grey horizontal bars show the different cloud periods 14a - e. The IPR concentration of about 25 L^{-1} (0.3 µm - 1 µm) and the total particle concentration (0.3 µm - 32 µm) had their maximum during cloud period 14a. The IPR concentration only slightly decreased, remaining at a relatively high level, until 14c, before coming close to 14a again during cloud period 14d. At the same time, the total ambient particle concentration (0.3 µm - 32 µm) during 14c reached its minimum within the cloud event before the concentration increased again during 14d. During cloud period 14e the total ambient particle concentration remains almost constant, whereas the strongly decreasing IPR concentration indicates the end of the cloud event. The temperature measured at the JFJ shows only slight fluctuations between 14a and 14b, whereas it started to decrease from 14c on. Since the temperatures between 14a and 14e were measured inside the cloud, the temperature always depends to a certain extent on the changing cloud characteristics and the amount of existing water vapor. The size distributions measured during the cloud periods 1a-e are shown in Fig. S14.

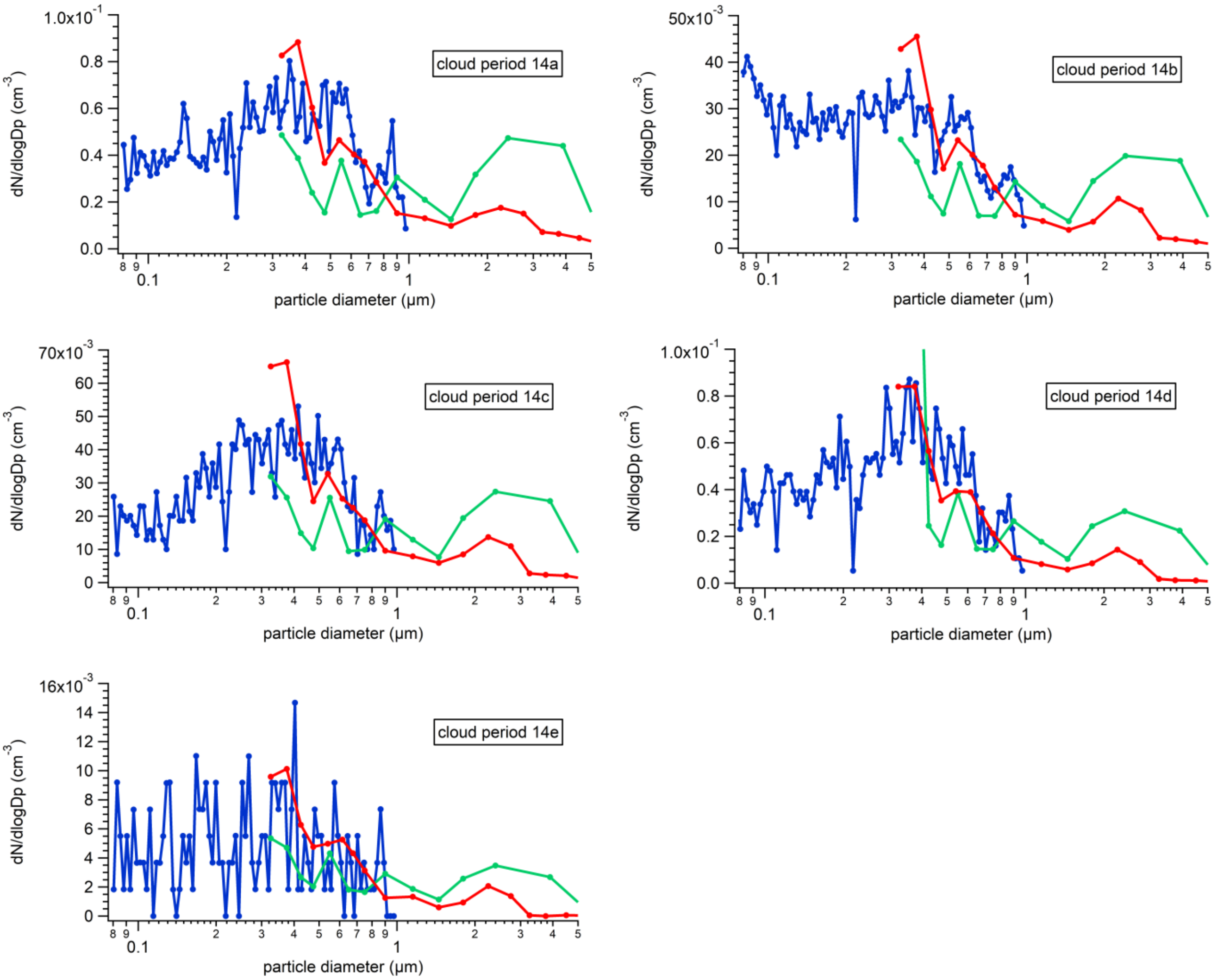

Figure S13: IPR number size distribution averaged as sub-periods of cloud event 14 when IPR properties were rather constant. Blue, green and red lines denote results from the UHSAS, OPS and Sky-OPC.

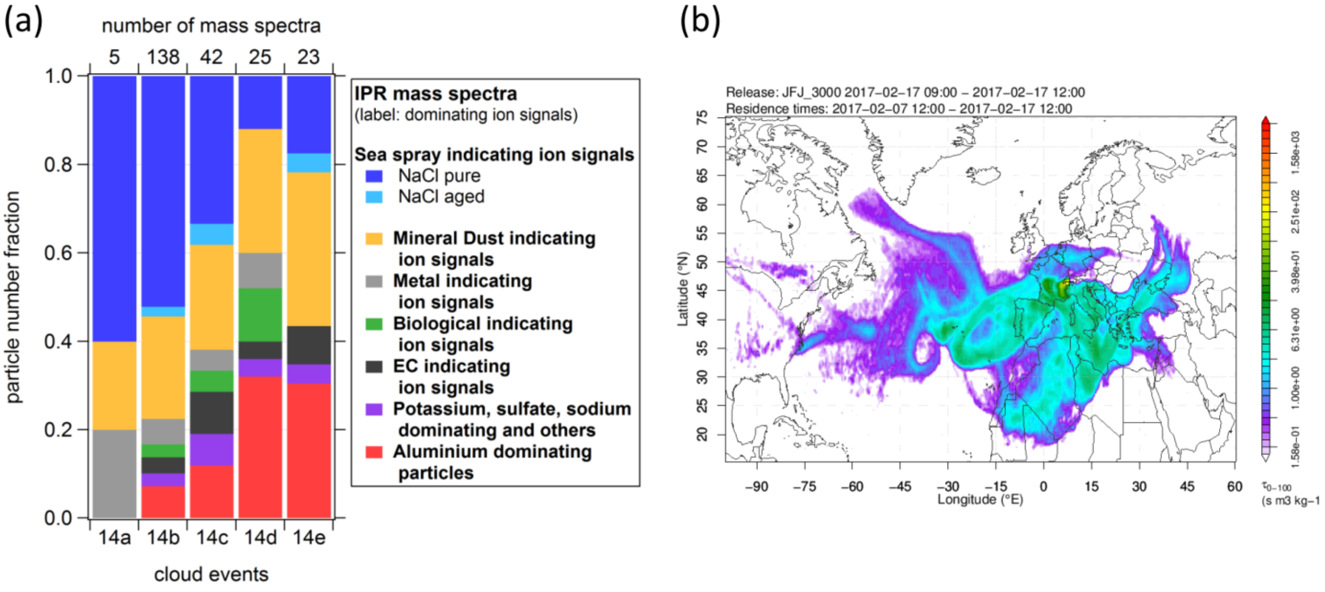

Figure S14: (a) Temporal evolution of the IPR fractions during the same cloud event as discussed in Fig. S12 (cloud event 14 at 17.02.2017 between 04:30 and 21:20), separated in five cloud periods (see more details Tab. S3). The pure NaCl type dominated the measured IPR composition at the beginning of the cloud event (cloud period 14a), before its fraction gradually decreased over time. (b) The source sensitivities at the surface determined by FLEXPART-COSMO are shown here as a footprint plot, calculated for 10 days backward for a release time at JFJ at 17.02.2017, 09:00 – 12:00. These data indicate an increased marine influence from the Atlantic Ocean and the Mediterranean Sea during this cloud event, which is a possible explanation for the presence of the pure and aged NaCl IPR type.

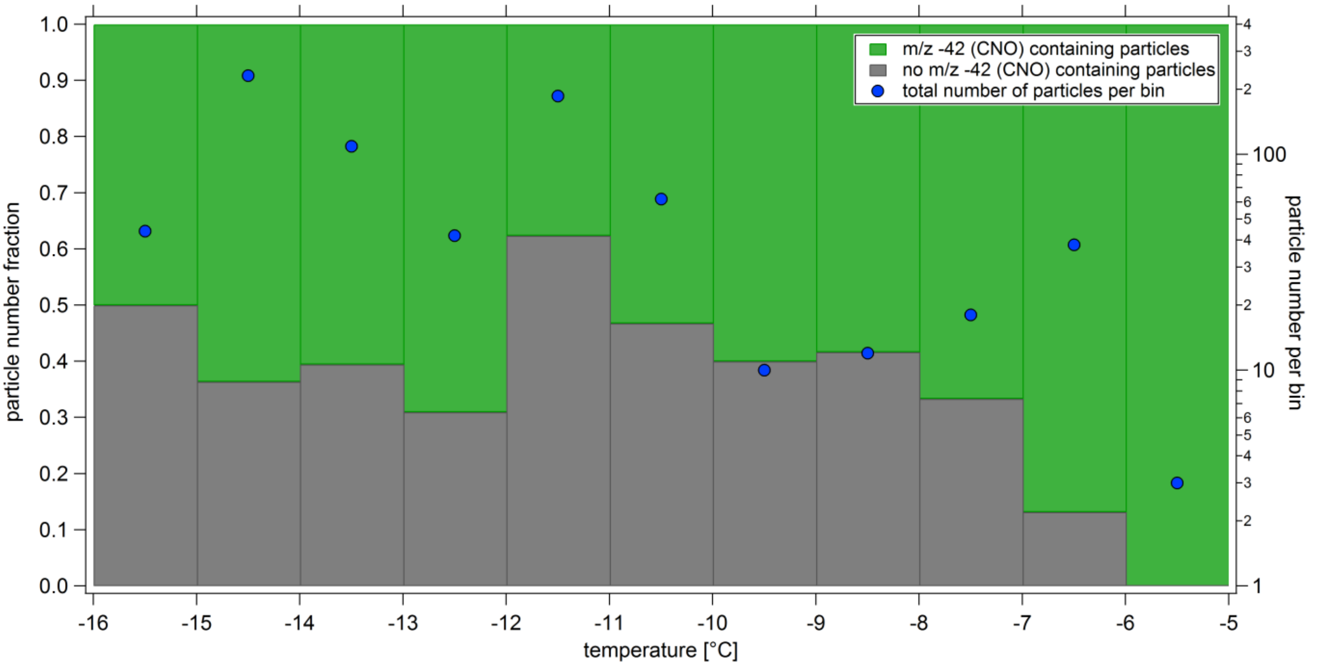

Figure S15: Number fraction of particles containing CNO^- (m/z 42) and of particles not containing CNO^- detected by the ALABAMA as a function of ambient temperature (1-K intervals) during all cloud events. The ion m/z 42 (CNO^-) was used because it was frequently detected in analyses of particles of biological origin (e.g. Clemen et al., 2020; Marsden et al., 2019; Cornwell et al., 2019; Zawadowicz et al., 2017; Pratt et al., 2009, Schmidt et al., 2017). An increasing fraction of the particle spectra contains a signal at 42 (CNO^-) with increasing temperatures. The ice activation at temperatures around -15 to -13°C for dust particles could be explained by traces of biogenic material, because surface dust frequently contains biological material (e.g., Conen et al., 2011; Fröhlich-Novoisky et al., 2015; O'Sullivan et al., 2014; Zawadowicz et al., 2017). Furthermore, the observation that CNO^- could have an influence on ice activity is supported by the correlation analysis of the n_s-time series with the m/z values (see Sect. 3.3), where m/z 42 was the anion with the highest correlation coefficient with n_s (for ALABAMA) in both method 1 and method 2 (see Fig. 4 in the main text).

Table S1: List of FLEXPART country specific selection of desert surface areas, with partially semi-arid or arid areas.

Bahrain	Oman	Libya
Gaza Strip	Qatar	Mali
Iran	Saudi Arabia	Mauritania
Iraq	Syria	Morocco
Iraq Saudi Arabia Neutral Zone	United Arab Emirates	Niger
Israel	Algeria	Senegal
Jordan	Cape Verde	Sudan
Kuwait	Chad	Tunisia
Lebanon	Egypt	Western Sahara

Table S2: Dates, duration and mean IPR number concentration in different particle size ranges of cloud periods with a lower contribution of small IPR (see also Fig. S10). Numbers are inferred from a) UHSAS, b) OPS and c) SKY-OPC measurements.

period	beginning	ending	duration [hh:mm:ss]	N_{IPR} [L^{-1}]a) (0.08-0.3 µm)	N_{IPR} [L^{-1}]a) (0.3-1.0 µm)	N_{IPR} [L^{-1}]b) (0.3-1.0 µm)	N_{IPR}[L^{-1}]c) (0.3-1.0 µm)	N_{IPR} [L^{-1}]b) (1.0-5.0 µm)	N_{IPR} [L^{-1}]c) (1.0-5.0 µm)
1c	27.01.2017 07:00:02	27.01.2017 09:09:52	02:09:50	13.3	14.6	11.5	14.0	6.0	3.0
3c	30.01.2017 16:31:02	31.01.2017 00:59:50	08:28:48	1.2	2.9	2.4	3.2	1.4	0.7
4a	31.01.2017 16:17:03	31.01.2017 21:31:52	05:14:49	0.9	2.6	2.2	2.6	1.4	0.5
5a	02.02.2017 10:40:04	02.02.2017 20:54:52	10:14:48	1.1	1.4	1.4	1.8	0.7	0.3
6	03.02.2017 16:44:02	03.02.2017 23:21:51	06:37:49	2.6	3.2	2.7	2.4	1.3	0.3
7b	04.02.2017 18:09:08	04.02.2017 19:40:57	01:31:50	1.8	2.7	3.3	3.6	1.3	0.7
8b	06.02.2017 00:00:02	06.02.2017 15:22:59	15:22:57	1.8	2.0	2.5	2.4	0.9	0.4
16c	21.02.2017 11:01:01	21.02.2017 14:19:50	03:18:49	4.0	4.1	3.9	4.3	1.8	0.7
duration weighted mean (all)			52:59:40	1.7	2.5	2.3	2.6	1.0	0.4

Table S3: Dates, duration and mean IPR number concentration in different particle size ranges of cloud periods with a higher contribution of small IPR (see also Fig. S11). The cloud periods 3b, 4b, 14b, 15 approached the measurement site from north west (NW) and the cloud periods 11a, 11b, 11d, 12a from south east (SE). Same information of duration averaged cloud periods (all periods, NW and SE events) are given at the bottom. Numbers are inferred from a) UHSAS, b) OPS and c) SKY-OPC measurements.

period	beginning	ending	duration [hh:mm:ss]	N_{IPR} [L^{-1}]a) (0.08-0.3 µm)	N_{IPR} [L^{-1}]a) (0.3-1.0 µm)	N_{IPR} [L^{-1}]b) (0.3-1.0 µm)	N_{IPR} [L^{-1}]c) (0.3-1.0 µm)	N_{IPR} [L^{-1}]b) (1.0-5.0 µm)	N_{IPR} [L^{-1}]c) (1.0-5.0 µm)
3b	30.01.2017 10:33:09	30.01.2017 13:44:59	03:11:50	10.9	6.9	5.7	3.2	1.4	0.7
4b	31.01.2017 22:56:03	01.02.2017 10:24:01	11:27:58	0.4	0.3	0.2	0.3	0.2	0.1
11a	10.02.2017 01:13:04	10.02.2017 02:59:53	01:46:50	35.8	23.2	26.1	25.1	11.4	5.0
11b	10.02.2017 03:00:03	10.02.2017 12:06:51	09:06:48	11.2	6.5	7.9	7.7	3.4	1.5
11d	10.02.2017 14:44:09	10.02.2017 16:53:58	02:09:50	5.8	4.1	4.3	3.6	1.2	0.5
12a	12.02.2017 03:30:06	12.02.2017 08:46:55	05:16:49	10.8	5.9	7.5	7.2	3.4	1.6
14b	17.02.2017 06:00:08	17.02.2017 12:05:57	06:05:49	16.6	11.7	11.0	13.0	6.0	3.1
15	20.02.2017 01:08:05	20.02.2017 02:42:54	01:34:50	6.1	4.8	5.7	5.2	1.7	0.7
duration weighted mean (all)			40:40:42	8.7	5.5	6.0	6.1	2.7	1.3
duration weighted mean (NW)			22:20:27	5.3	3.7	3.5	4.0	1.8	0.9
duration weighted mean (SE)			18:20:15	12.8	7.7	9.1	8.8	3.9	1.8

Table S4: Dates, duration and mean IPR number concentration in different particle size ranges of sub periods of cloud event 14. Numbers are inferred from a) UHSAS, b) OPS and c) SKY-OPC measurements.

period	beginning	ending	duration [hh:mm:ss]	N_{IPR} [L^{-1}]a) (0.08-0.3 µm)	N_{IPR} [L^{-1}]a) (0.3-1.0 µm)	N_{IPR} [L^{-1}]b) (0.3-1.0 µm)	N_{IPR} [L^{-1}]c) (0.3-1.0 µm)	N_{IPR} [L^{-1}]b) (1.0-5.0 µm)	N_{IPR} [L^{-1}]c) (1.0-5.0 µm)
14a	17.02.2017 04:35:08	17.02.2017 05:59:58	01:24:50	25.0	25.4	23.5	26.2	13.9	6.7
14b	17.02.2017 06:00:08	17.02.2017 12:05:57	06:05:49	16.6	11.7	11.0	13.0	6.0	3.1
14c	17.02.2017 12:06:07	17.02.2017 14:15:56	02:09:49	15.1	16.4	15.2	18.5	8.1	4.2
14d	17.02.2017 16:40:03	17.02.2017 18:42:52	02:02:49	24.6	24.3	--	23.7	--	3.8
14e	17.02.2017 18:44:02	17.02.2017 21:14:52	02:30:50	2.7	2.3	2.6	2.9	1.0	0.5

References

Clemen, H.-C., Schneider, J., Klimach, T., Helleis, F., Köllner, F., Hünig, A., Rubach, F., Mertes, S., Wex, H., Stratmann, F., Welti, A., Kohl, R., Frank, F., and Borrmann, S.: Optimizing the detection, ablation, and ion extraction efficiency of a single-particle laser ablation mass spectrometer for application in environments with low aerosol particle concentrations, Atmos. Meas. Tech., 13, 5923-5953, 10.5194/amt-13-5923-2020, 2020.

Conen, F., Morris, C. E., Leifeld, J., Yakutin, M. V., and Alewell, C.: Biological residues define the ice nucleation properties of soil dust, Atmos. Chem. Phys., 11, 9643-9648, 10.5194/acp-11-9643-2011, 2011.

Cornwell, G. C., McCluskey, C. S., Levin, E. J. T., Suski, K. J., DeMott, P. J., Kreidenweis, S. M., and Prather, K. A.: Direct Online Mass Spectrometry Measurements of Ice Nucleating Particles at a California Coastal Site, Journal of Geophysical Research: Atmospheres, 124, 12157-12172, 10.1029/2019JD030466, 2019.

Fröhlich-Nowoisky, J., Hill, T. C. J., Pummer, B. G., Yordanova, P., Franc, G. D., and Pöschl, U.: Ice nucleation activity in the widespread soil fungus Mortierella alpina, Biogeosciences, 12, 1057 -1071, 10.5194/bg-12-1057-2015, 2015.

Herrmann, E., Weingartner, E., Henne, S., Vuilleumier, L., Bukowiecki, N., Steinbacher, M., Conen, F., Collaud Coen, M., Hammer, E., Jurányi, Z., Baltensperger, U., and Gysel, M.: Analysis of long-term aerosol size distribution data from Jungfraujoch with emphasis on free tropospheric conditions, cloud influence, and air mass transport, J. Geophys. Res. Atmos, 120, 9459-9480, 10.1002/2015JD023660, 2015.

Marsden, N. A., Ullrich, R., Möhler, O., Eriksen Hammer, S., Kandler, K., Cui, Z., Williams, P. I., Flynn, M. J., Liu, D., Allan, J. D., and Coe, H.: Mineralogy and mixing state of north African mineral dust by online single-particle mass spectrometry, Atmos. Chem. Phys., 19, 2259-2281, 10.5194/acp-19-2259-2019, 2019.

O'Sullivan, D., Murray, B. J., Malkin, T. L., Whale, T. F., Umo, N. S., Atkinson, J. D., Price, H. C., Baustian, K. J., Browse, J., and Webb, M. E.: Ice nucleation by fertile soil dusts: relative importance of mineral and biogenic components, Atmos. Chem. Phys., 14, 1853-1867, 10.5194/acp-14-1853-2014, 2014.

Pratt, K. A., DeMott, P. J., French, J. R., Wang, Z., Westphal, D. L., Heymsfield, A. J., Twohy, C. H., Prenni, A. J., and Prather, K. A.: In situ detection of biological particles in cloud ice-crystals, Nature Geoscience, 2, 398, 10.1038/ngeo521, 2009.

Schmidt, S., Schneider, J., Klimach, T., Mertes, S., Schenk, L. P., Kupiszewski, P., Curtius, J., and Borrmann, S.: Online single particle analysis of ice particle residuals from mountain-top mixed-phase clouds using laboratory derived particle type assignment, Atmos. Chem. Phys., 17, 575-594, 10.5194/acp-17-575-2017, 2017.

Zawadowicz, M. A., Froyd, K. D., Murphy, D. M., and Cziczo, D. J.: Improved identification of primary biological aerosol particles using single-particle mass spectrometry, Atmos. Chem. Phys., 17, 7193-7212, 10.5194/acp-17-7193-2017, 2017.

Zellweger, C., Forrer, J., Hofer, P., Nyeki, S., Schwarzenbach, B., Weingartner, E., Ammann, M., and Baltensperger, U.: Partitioning of reactive nitrogen (NOy) and dependence on meteorological conditions in the lower free troposphere, Atmos. Chem. Phys., 3, 779 - 796, 10.5194/acp-3-779-2003, 2003.